Research Article

Environmental Chemistry and Safety
DOI: 10.26599/ECS.2026.9600004
2026, 2, 9600004

Vacancy-Induced Electron Redistribution Boosts NO_2 Sensing in CdSe Nanoplatelets via Defect-Mediated Charge Transfer

Yan Zhang[1†], Yunjiang Zhang[1†], Junjun Sun[1], Cong Qin[1], Dongping Xue[1], Jianliang Cao[1,2,3], and Yan Wang[2,4*]

[1]College of Chemistry and Chemical Engineering, Henan Polytechnic University, Jiaozuo, 454000, China

[2]State Collaborative Innovation Center of Coal Work Safety and Clean-efficiency Utilization, Henan Polytechnic University, Jiaozuo 454000, China

[3]Zhengzhou Institute for Advanced Research of Henan Polytechnic University, Zhengzhou 450015, China

[4]Henan Province Engineering Technology Research Center of Explosion Dynamic Disaster Early Warning and Emergency, Henan Polytechnic University, Jiaozuo 454000, China

Abstract: Defect engineering is crucial for enhancing gas sensors, however, the mechanism by which vacancies amplify sensing signals remains unclear. This study synthesizes hexagonal CdSe nanoplatelets with tunable vacancy density through a NaOH-regulated hydrothermal and calcination process. The optimized sensor demonstrates an outstanding response (R_g/R_a=9.03) to 10 ppm of NO_2 at 120°C, showcasing remarkably quick response-recovery times of 12 and 13 s, respectively, along with an exceptionally low theoretical detection limit of 82.5 ppb. The DFT calculation results indicate that vacancies induce electron redistribution in CdSe, which helps promote charge transfer and enhance surface reactivity. In addition, NaOH regulation simultaneously optimized the material particle size and vacancy density, ensuring the dominant position of active sites in electron capture. This work highlights vacancy-induced electron redistribution as a key mechanism for boosting sensing performance and provides a viable defect-mediation strategy for advanced gas sensors.

Key words: CdSe; Grain size control; Se vacancies; NO_2 gas sensor; Low temperature

Citation: Zhang Y, Zhang Y J, Sun J J, et al. Vacancy-Induced Electron Redistribution Boosts NO_2 Sensing in CdSe Nanoplatelets via Defect-Mediated Charge Transfer. *Environmental Chemistry and Safety*, 2026, 2, 9600004. https://doi.org/10.26599/ECS.2026.9600004

1. Introduction

Currently, industrial emissions in developing countries generate hazardous air contaminants, threatening environmental sustainability and community well-being [1-3]. NO_2 is usually emitted into the atmosphere as a result of the combustion of fossil fuels, industrial production and road traffic [4, 5]. NO_2 has a serious ecological impact through reduced atmospheric visibility, acidification of surface water and the formation of acid rain [6-8]. In addition, NO_2 induces serious health effects in humans. Inhalation of small amounts of NO_2 can cause irritation of the respiratory mucosa, and prolonged exposure to excessive NO_2 concentrations can cause damage to human lung function and the cardiovascular system. In severe cases, it may induce cellular gene mutations, leading to cancer [9-11]. Hence, developing a sensor with high sensitivity and sustained effectiveness to detect low concentrations of NO_2 is essential.

Conventional metal oxide semiconductor (MOS) sensors typically exhibit limitations including high operating temperatures, poor selectivity, and high detection limits due to their wide bandgaps and low charge carrier mobility [12, 13]. Ideal gas-sensing devices require optimal selectivity, enhanced sensitivity, and cost-effectiveness. This necessitates the development of advanced sensors capable of detecting trace-level atmospheric NO_2 concentrations under low-temperature operating conditions [14]. Up to now, the emergence of two-dimensional (2D) nanomaterials, especially MXenes, transition metal dichalcogenides (TMDs) and metal carbides [15], has been extensively studied and is considered a promising material to detect NO_2 [16]. Most 2D nanomaterials demonstrate significant technological potential through tunable bandgaps, high carrier mobility, and rapid visible-light responsiveness, enabling applications in photovoltaics, thermoelectrics, photodetection, ultrafast dynamics, and gas sensing. Compared to other 2D nanomaterials, TMDs demonstrate distinct advantages in detecting NO_2 gas at low temperatures owing to their substantial surface-area-to-volume proportion, responsive interfaces, and superior electrical conductivity [17]. According to recent reports, researchers have developed many vacancy control methods to improve the low vacancy density of TMDs, thereby enabling the detection of NO_2 at low temperatures. Liu et al. created ZnSe/ZnO heterojunctions through high-temperature thermal oxidation. In comparison to pure ZnSe, the ZnSe/ZnO heterojunction exhibits a greater vacancy density, leading to a 7.3-fold enhancement in NO_2 detection relative to sensors utilizing ZnSe [18]. Wu et al. have doped Se into MoS_2 through thermal selenization. During the selenium doping process, sulfur vacancy defects are formed with high density, result-

†They are co-first authors.

Correspondence to: Wang Y, yanwang@hpu.edu.cn

Received: September 28, 2025; Revised: December 17, 2025; Accepted: January 4, 2026

ing in the sensor exhibiting superior performance at room temperature [19]. Utilizing a solvothermal technique, Yang and colleagues synthesized $SnSe_2$ nanosheets featuring two distinct morphologies that revealed an increased number of defects, resulting in a detection threshold of 200 ppb for NO_2 at ambient temperature [20].

Cadmium selenide (CdSe), recognized as a 2D transition metal disulfide semiconductor, has been widely investigated for applications in photocatalysis, photodegradation, and electrochemical sensing due to its suitable band gaps and favorable energy band configuration [21-25]. CdSe has a band gap of about 1.7 eV [26] and has a direct jump-type energy band structure [27]. However, CdSe has rarely been explored in gas-sensing applications in the current literature. Optimized NO_2 sensing materials require enhanced electrical conductivity coupled with preferential NO_2 adsorption energetics and suppressed cross-sensitivity to interferents [28]. Computational studies have demonstrated that transition metal elements (Cd) [29] and chalcogen elements (Se) [30] exhibit superior NO_2 binding affinities due to their distinctive d-orbital electron configurations [31].

Inspired by the above findings, a sensor for low-temperature detection of NO_2 using CdSe nanomaterials has been reported. Hexagonal CdSe stacked layers are synthesized by hydrothermal method and subsequent annealing treatment. By changing the concentration of NaOH added, the grain size and vacancy density of different CdSe samples can be adjusted, which has been confirmed through XRD and EPR analysis. The findings indicate that the sensor utilizing CS-0.7 demonstrates superior performance for NO_2 at a concentration of 10 ppm, achieving a response value as high as 9.03, a quick response-recovery time of 5 and 10 s, and a lower actual detection threshold of 0.1 ppm. A comprehensive examination of the sensitization mechanism for NO_2 has been conducted.

2. Experimental

2.1. Synthesis of CdSe

CdSe was synthesized using a conventional one-step hydrothermal approach combined with a thermal treatment process, as illustrated in Fig. 1a. To prepare solution A, 2 mmol of $CdCl2 \cdot 2.5H_2O$ was dissolved in 20 mL of deionized water (DI). Meanwhile, solution B was created by dissolving 2 mmol of Na_2SeO_3 in another 20 mL of DI. The next step involved mixing solutions A and B, which were then sonicated for 10 min until a layered appearance was observed. Following this, 15

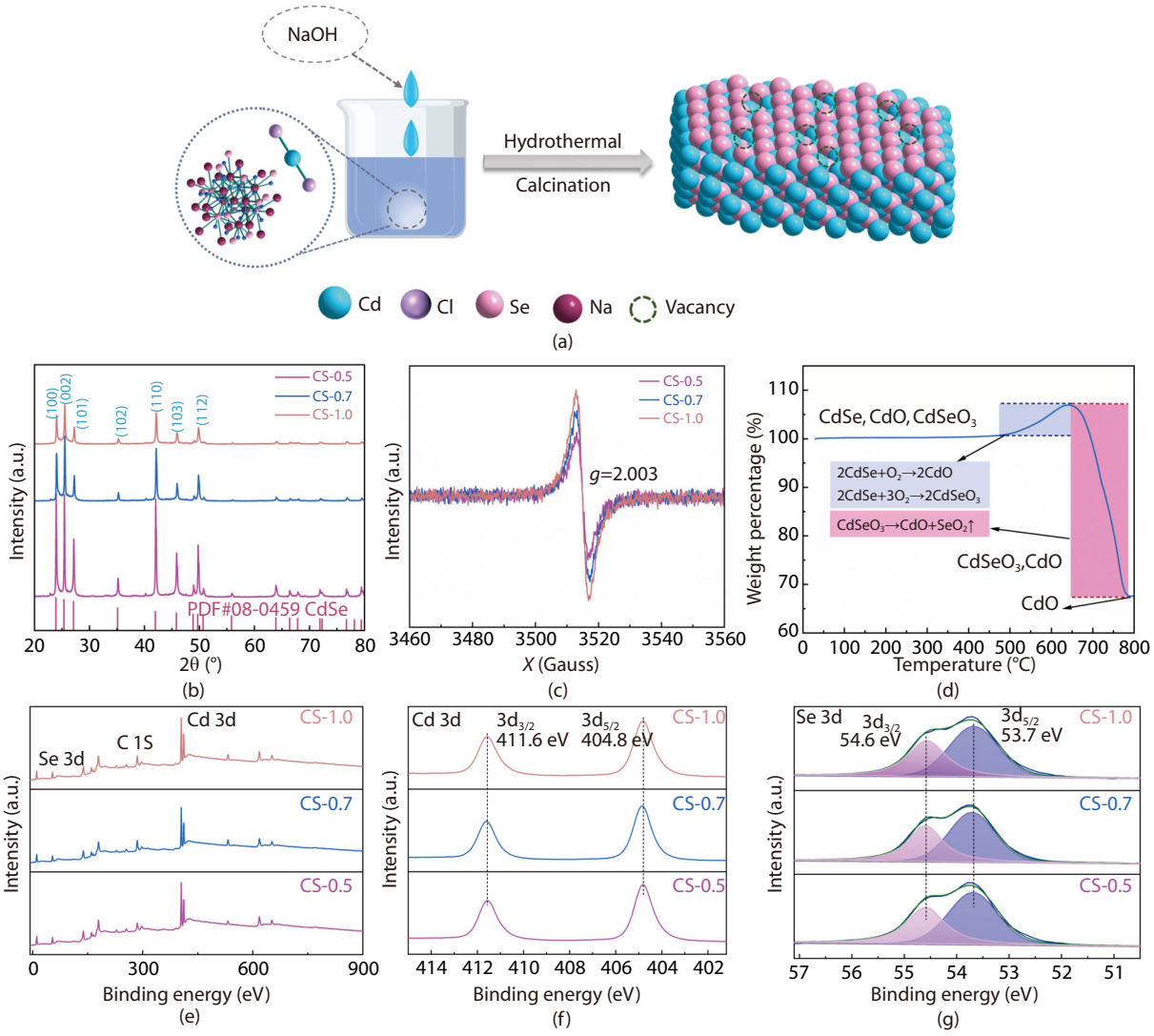

Fig. 1. (a) Diagram of the synthesis process of CdSe, (b) XRD patterns of CdSe, (c) EPR curves of CS-0.5, CS-0.7 and CS-1.0, (d) TGA curves of CdSe, (e) XPS spectra of CdSe. (f) High-resolution Cd 3d, (g) Se 3d spectra.

mL of NaOH solution at varying concentrations (0.5, 0.7, 1.0 mM, the percentage contents of mass are 2.4%, 3.4%, and 4.7%, respectively) was introduced into the precursor solution, along with the addition of 20 mL of ethylene glycol (EG), and the mixture was stirred magnetically for 30 minutes. Afterward, the precursor solution was processed through hydrothermal synthesis in a 100 mL Teflon reactor, maintaining a temperature of 180°C for 24 h. Once cooled to ambient temperature, the ensuing precipitate underwent several washing cycles with deionized water and ethanol to remove ionic impurities, followed by drying at 60°C. Finally, pure CdSe was achieved by calcining at 300°C for 2 h in an argon environment within a tube furnace. The final products were labeled as CS-0.5, CS-0.7, and CS-1.0, reflecting the different quantities of NaOH used.

2.2. Characterization and DFT methods

The characterization of materials and theoretical calculation methods can be found in the Supporting Information.

2.3. Gas sensing tests

The raw material, approximately 5 mg, was applied to the intertwined silver-palladium electrodes (13.4 mm×7.0 mm) using deionized water and allowed to age at 60°C for 18 h to create the sensor. The CGS-MT system (Beijing Elite Tech Co., Ltd. in China) was utilized to capture the test data. Throughout the testing process, all analytical gas species were maintained in the vapor phase, and the concentrations of the analytes were quantified using volumetric dosing calculations based on eq.1 [32]:

$$C_1V_1 = C_2V_2 \quad (1)$$

Among these, C_1 and C_2 (ppm) refer to the concentrations of the precursor gas and the necessary gas, respectively. V_1 and V_2 (5400 mL) respectively represent the target gas volume and the test chamber volume. The Relative humidity is controlled by saturated salt solution. $MgCl_2$, K_2CO_3, $Mg(NO_3)_2$, NaCl, $CuCl_2$, KCl represent the Relative humidity of 32.8%, 43%, 54.3%, 67%, 75.3%, 85%, respectively [33, 34]. The formulation of this response is articulated in eq.2 [35]:

$$Y=R_g/R_a \quad (2)$$

Where R_a and R_g represent the sensor resistance in air and after target gas exposure, respectively.

3. Result and discussion

3.1. Material characterizations

The synthesized CdSe nanomaterials underwent analysis via X-ray diffraction (XRD) to ascertain their crystalline phase structure. As illustrated in Fig. 1b, the distinct peaks observed in the samples align closely with the crystal phases of hexagonal CdSe, specifically (100), (002), (101), (102), (110), (103), and (112) (PDF No. 08–0459) [26]. It is evident from Fig. 1b that an increase in NaOH content (from 2.4% to 4.7%) leads to a noticeable reduction in the intensity of the diffraction peaks across the three materials. To further explore the impact of NaOH concentrations on the crystalline phase of CdSe, a comparison of the full width at half maximum (FWHM) and crystallite size among the three samples was conducted.

According to Table 1, the FWHM values for the (100) plane in CS-0.5, CS-0.7, and CS-1.0 are 0.182, 0.214, and 0.210, respectively, with CS-0.7 exhibiting the maximum FWHM among the three samples analyzed. The crystallite sizes were assessed using the equation ($D = 0.89\lambda/\beta\cos\theta$) applied to the XRD patterns [36]. The resulting dimensions for the (100) facets of the three samples are 3.7039 nm, 3.6855 nm, and 3.6930 nm, in that order. It can be clearly observed that CS-0.7 has the smallest grain size. Smaller grain sizes could provide more grain boundaries, which favor the reaction of gas molecules on the surface of the material [37]. In novel semiconductor materials, parameters such as lattice strain and dislocation width are often utilized to evaluate electron mobility [38]. The lattice strain and dislocation density for the three samples have been calculated. From Table 1, it can be seen that the values of lattice strain and dislocation width for CS-0.7 are 0.00147 and 0.00464, respectively, which are the highest among the samples analyzed. This indicates that CS-0.7 demonstrates superior electron mobility and can significantly improve gas-sensing performance at lower temperatures.

Table 1. FWHM, crystallite size, lattice strain and dislocations of the materials.

	CS-0.5	CS-0.7	CS-1.0
FWHM	0.182	0.214	0.210
Peak position (θ_{hkl}(°))	11.97	12.01	12.01
Crystallite size (nm)	3.7039	3.6855	3.6930
β_{hkl}**(rad)**	0.0255	0.0276	0.0223
ε^{SH}	0.00135	0.00147	0.00119
δ^{SH}**(line/nm²)**	0.00396	0.00464	0.00328

ε^{SH}: lattice strain, δ^{SH}: lattice dislocation density.

The impact of NaOH addition on selenium vacancies in CdSe is investigated through the evolution of EPR images. As illustrated in Fig. 1c, the EPR signal observed at g = 2.003 is linked to the existence of Se vacancies [39, 40], where CS-1.0 displays the most prominent signal, indicating that it has the greatest concentration of Se vacancies. Furthermore, the EPR signals for the CdSe samples became more pronounced as NaOH concentration increased, suggesting that the alkali treatment effectively improved the selenium vacancy concentration.

To assess the thermal stability of the CdSe nanomaterials, TGA analyses were performed on CS-0.7. The results of the experiments are illustrated in Fig. 1d, where CdSe experiences thermal treatment in ambient air between 30 and 800°C with a consistent ramp rate of 10°C/min. Furthermore, CdSe was subjected to calcination in an air environment at temperatures of 500°C, 650°C, and 800°C, with their corresponding XRD images displayed in Fig. S1. The TGA curves indicate that CdSe maintains significant stability below 500°C, showing minimal mass loss. Conversely, from 500°C to 640°C, an upward trend in the sample's mass is observed. This mass fluctuation is attributed to the atmospheric oxidation of CdSe into $CdSeO_3$ and CdO (see Fig. S1a and b). A notable mass loss of 39.383% occurs between 640°C and 785°C, during which CdSe and $CdSeO_3$ are fully oxidized to CdO, altering the mass of the sample. The thermal analysis indicates that there is little to no mass loss past 785°C, confirming complete oxidation of CdSe at this temperature threshold (refer to Fig. S1c).

Additionally, the valence states and core-level electronic

configurations of Cd and Se in CdSe nanostructures (CS-0.5, CS-0.7, CS-1.0) are characterized by XPS profiles (Fig. 1e-g). The gross spectra of the three samples, depicted in Fig. 1e, confirm the presence of elemental Cd and Se. In Fig. 1f, the high-resolution XPS spectrum for Cd 3d reveals characteristic doublet peaks at 404.8 eV ($3d_{5/2}$) and 411.6 eV ($3d_{3/2}$), which are associated with the Cd-Se bonding states within the CdSe system [41]. As illustrated in Fig. 1g, the Se 3d XPS spectra for the three samples are divided into two subpeaks, with the lattice states of Se $3d_{5/2}$ and $3d_{3/2}$ in CdSe showing binding energies of 53.7 eV and 54.6 eV, respectively. The variation of Se 3d peak area is mainly caused by the different vacancy concentrations of the material. [42].

Fig. 2a-f displays the SEM images for the samples CS-0.5, CS-0.7, and CS-1.0. In Fig. 2a and d, the SEM images of CS-0.5 are shown at magnifications of 1 μm and 200 nm. The SEM images for CS-0.7 at the same magnifications are presented in Fig. 2 4b and e. Similarly, Fig. 2c and f feature the SEM images of CS-1.0, also at 1 μm and 200 nm sizes. Analysis of the SEM images indicates minimal differences in the morphology of the three samples, with the morphology arising from the stacking of nanoscale hexagonal lamellar structures. The lattice spacing measured from the HRTEM image of CS-0.7 is determined to be 0.352 nm in Fig. 2g. As per the XRD standard card for CdSe (JCPDS No. 08-0459), this spacing corresponds to the (002) crystalline plane of hexagonal CdSe. Fig. 2h-j show the scanning TEM (STEM) images of partial region for CS-0.7, from which we can observe Cd and Se elements are evenly dispersed all over the whole nanosheets region.

The surface areas of samples CS-0.5, CS-0.7 and CS-1.0 are calculated by BET analysis. Fig.S2a-c illustrate the N_2 adsorption-desorption isotherms for the three samples. The linear isotherm profile reveals characteristic type IV behavior, indicating initial monolayer adsorption followed by multilayer formation within mesoporous structures [43]. The specific surface areas of CS-0.5, CS-0.7 and CS-1.0 are calculated to be 4.271, 4.324 and 5.982 m^2/g, respectively. The three CdSe samples exhibit enhanced specific surface areas correlating with elevated NaOH concentrations. The pore sizes of the three materials are mainly distributed between 10-35 nm, with average pore sizes of 26.1682, 27.0427, and 27.0427 nm, respectively, indicating that the materials are all mesoporous structures.

3.2. NO_2 sensing performance of CdSe

The variation in resistance for three sensors was evaluated, with results at different operating temperatures shown in Fig. 3a. Due to the thermally induced enhancement of charger-carrier density and mobility, the resistance values of sensors are negatively correlated with temperature [44]. In Fig. 3b, the response changes in the sensor array as a function of operational temperature are depicted. The gas sensing assessment included CS-0.5, CS-0.7, and CS-1.0 sensors that were subjected to 10 ppm NO_2 within a temperature range of 70°C to 180°C. Between 70°C and 120°C, the responses of the three sensors increased with rising temperature. Conversely, a downward trend in response values was noted among the sensors in the 120°C to 180°C range as temperatures continued to rise. This is mainly because the increase in temperature provides the necessary activation energy for the adsorption of NO_2 and the reaction of active oxygen species, thereby improving the response value of the sensor. At the optimal temperature, the adsorption and desorption of gas reach kinetic equilibrium, at which point the response value is highest. Due to the fact that gas adsorption is usually an exothermic process, as the temperature continues to rise, the equilibrium coverage of gas molecules on the surface sharply decreases, and the desorption rate is fast, resulting in a decrease in the total charge transfer amount and a decrease in the response value [45-47]. The maximum response values for CS-0.5, CS-0.7, and CS-1.0 sensors were all attained at 120°C, establishing this temperature as the optimal operating point for the CdSe sensors. Furthermore, throughout the entire temperature spectrum, the CS-0.7 sensor consistently exhibited higher response values compared to both the CS-0.5 and CS-1.0 sensor. Fig. 3c illustrates the restoration of dynamic response among three detectors exposed to 10 ppm NO_2 at 120°C. The response figures for the CS-0.5, CS-0.7, and CS-1.0 sensors are 5.62, 9.03, and 2.99, with response and recovery durations of 22/12, 12/13, and 25/17 s,

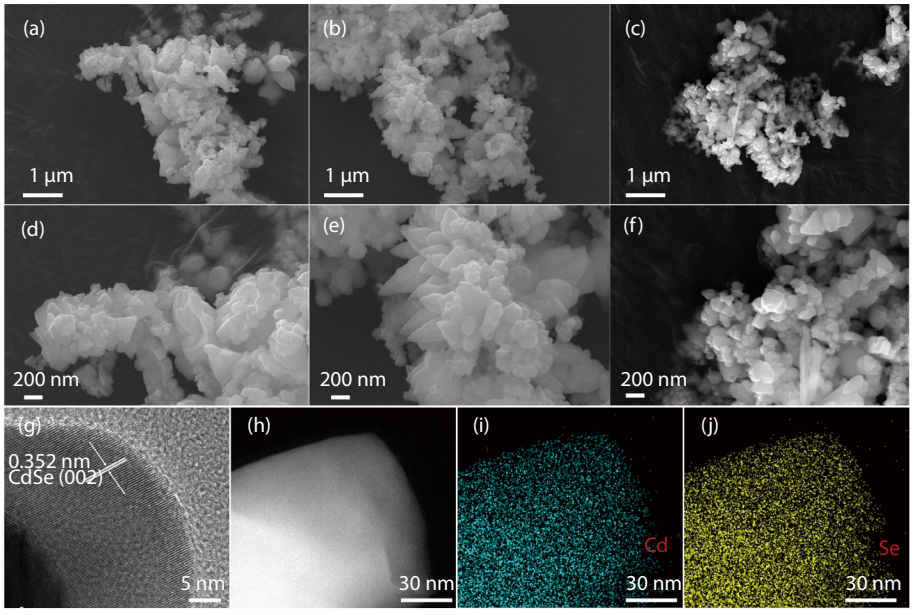

Fig. 2. SEM images of (a,d) CS-0.5, (b,e) CS-0.7, (c,f) CS-1.0, (g) HRTEM images of CS-0.7, (h-j) Elemental mapping images of CS-0.7.

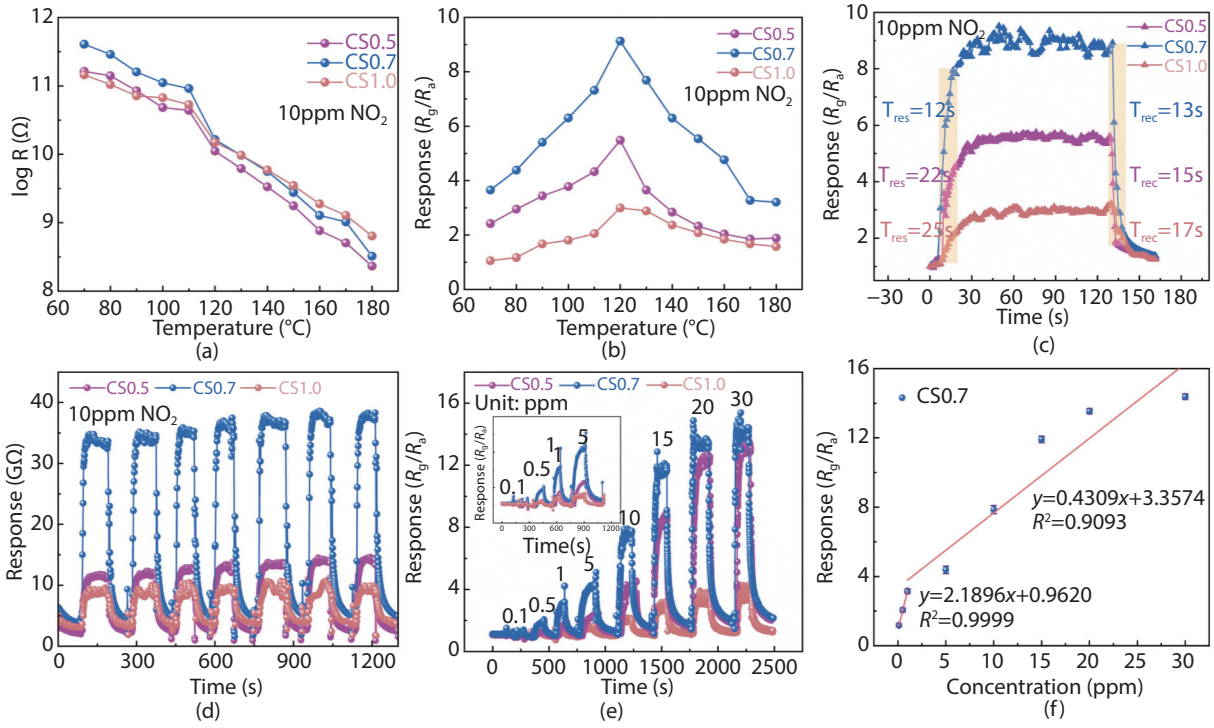

Fig. 3. Resistance (a) and responses (b) of sensors at various temperatures. (c) The response-recovery time of sensors to 10 ppm NO_2 at 120°C. (d) the repeatability tests. (e) Response-recovery curves at different concentrations. (f) Linear relationship between concentration and response value.

respectively. Notably, the CS-0.7 sensor exhibits the highest response value alongside the shortest response and recovery intervals. This improvement in performance may be attributed to the synergistic effect of small grain size and vacancies, which significantly enhances the gas performance of the materials [48]. The repeatability of the three sensors at 120°C when detecting NO_2 was evaluated, as depicted in Fig. 3d. The results show that after performing seven consecutive cyclic tests, all three sensors exhibited stability, enabling their resistance values to return to the initial measurement. This outcome demonstrates the reliability and precision of the sensors. Fig. 3e provides insight into the response dynamics of the CS-0.5, CS-0.7, and CS-1.0 sensors in response to NO_2 concentrations ranging from 0.1 to 30 ppm. In assessments across various gas concentrations, the CS-0.7 sensor yielded the most favorable outcome, displaying a response of 14.28 for 30 ppm NO_2, surpassing the performance of both the CS-0.5 and CS-1.0 sensors. Additionally, evaluations were conducted to observe the responses of the CS-0.5, CS-0.7, and CS-1.0 sensors to NO_2 concentrations ranging from 100 ppb to 5 ppm (inserted in Fig. 3e), with the CS-0.7 sensor exhibiting a response value of 1.29 for 100 ppb NO_2. Fig. 3f showcases the linear curves of the CS-0.7 sensor across the range of 100 ppb to 30 ppm. For 100 ppb-1 ppm, Y (Response) and x (concentration) can be described as: y=2.1885x+0.9628 (R^2=0.9999). For 1-30 ppm, it can be described as: y=0.4288x+3.4152 (R^2=0.8940). The theoretical detection limit (DL) is calculated through the formula [49]:

$$DL = 3(rms/slop) \quad (3)$$

$$rms = \left(\sum(R_i-1)^2)/N\right)^{1/2} \quad (4)$$

rms represents the root mean square of response fluctuations at 30 points at the baseline in the absence of target gas, while *slope* was calculated from Fig. 3f. R_i represents the response value prior to the introduction of gas, while N refers to the number of data points. The DL for CS-0.7 is established at 82.5 ppb. The fitted curves assessed at higher NO_2 concentrations demonstrated a significant flattening, indicative of the gradual saturation of primary adsorption sites on the surface when exposed to elevated concentrations [50, 51].

Furthermore, the selectivity of the sensors towards different gas species has been investigated [14]. The response values for three sensors in relation to 10 ppm NO_2 and a mixed gas comprising 5 ppm NO_2 along with 500 ppm of various typical hazardous gases (H_2, C_2H_4, NH_3, H_2S, CH_4, and CO) at 120°C is illustrated in Fig. 4a. It is evident that even with high levels of interfering gases present, the CdSe sensor maintains a significant response value for NO_2. This demonstrates the impressive selectivity of the CdSe sensor for NO_2. A significant challenge that resistive sensors currently face is the ability to maintain stable performance in high humidity environments. In conditions of elevated humidity, the initial resistance tends to decrease considerably as water molecules physically adhere to gas-sensing substrates, depleting surface oxygen species and producing a significant amount of $H3O^+$ that releases electrons [52]. To control the relative humidity, the test chamber was filled with varying concentrations of several saturated solutions. In Fig. 4b, c, the baseline resistance and response variation of the CS-0.7 sensor to 10 ppm NO_2 at 120°C with 31-94% relative humidity are displayed. The resistance of the sensor changes slightly at relative humidity below 76%, and the response value remains essentially constant, proving the excellent humidity resistance of the CS-0.7 sensor. When the relative humidity is above 76%, at this point the response and resis-

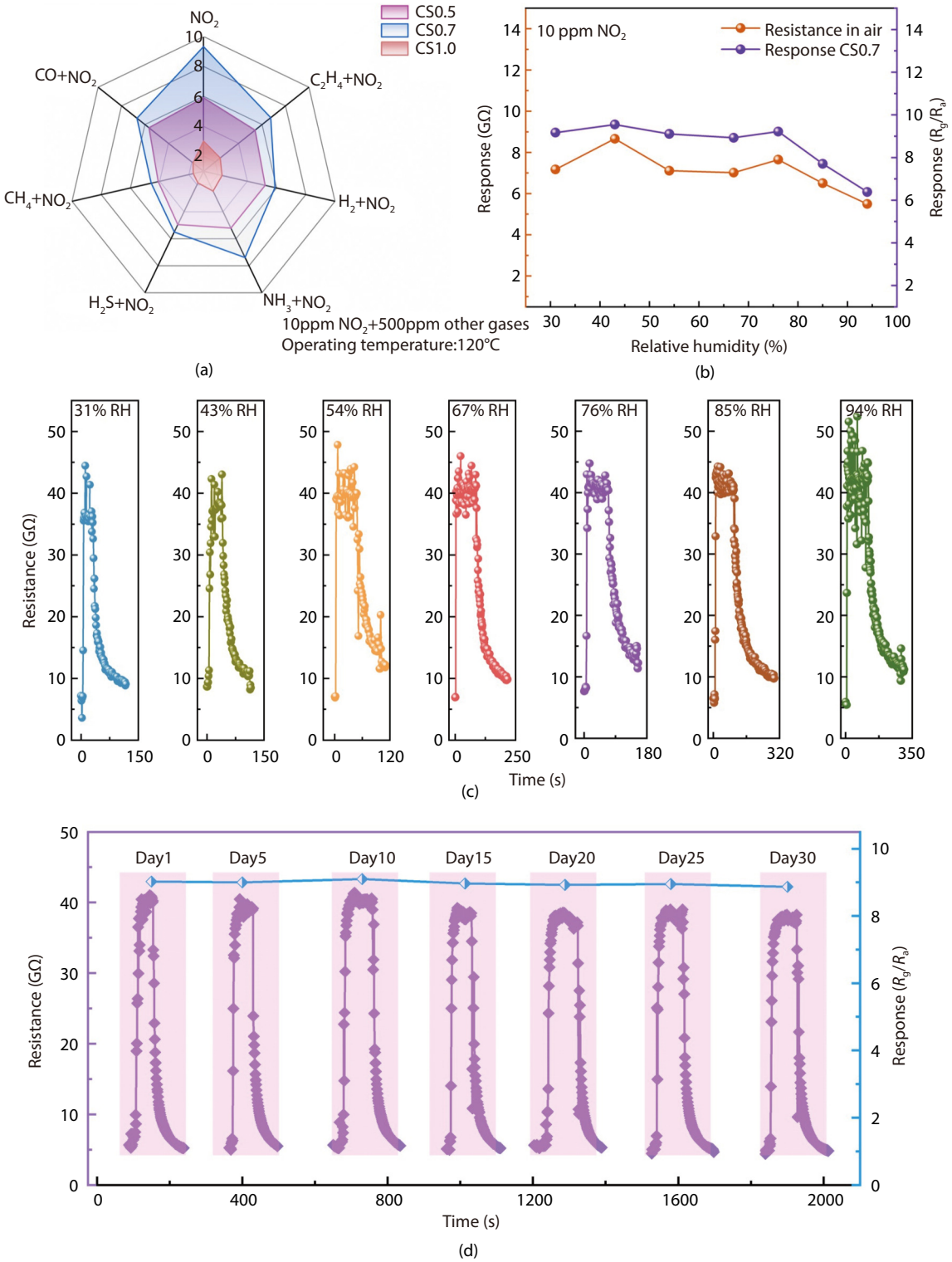

Fig. 4. (a) Selectivity of sensors for 10 ppm NO_2 and 500 ppm interfering gasat 120°C, (b) Response of the CS-0.7 sensor and baseline resistance change in air at different humidity, (c) Dynamic response recovery curves, (d) Long-term stability of the CS-0.7 sensor over 30 days.

tance values of the CS-0.7 sensor decrease simultaneously as the relative humidity increases. This is due to water molecules adsorbing on the surface of the material, forming hydroxyl groups and injecting electrons into the material's conduction band, thereby leading to a decrease in baseline resistance. This process competes with NO_2 adsorption, resulting in a reduced response value under high humidity conditions. [53]. However, as the relative humidity reached 94% finally, the response value of CS-0.7 sensor for 10 ppm NO_2 was still 6.37, which demonstrated the stability and reliability of CS-0.7 sensor for NO_2 detection under humid conditions.

By performing a conventional cycle every five days, the NO_2-responsive resistance dynamics of the CS-0.7 sensor were carefully analyzed at a concentration of 10 ppm (see Fig. 4d). After a period of 30 days, the CS-0.7 sensor's response to NO_2 across various concentrations remained above approximately 90% of its initial values. The dynamic characteristics of the CS-0.7 sensor showed no significant degradation and continued

to provide a consistent and rapid response to NO_2, as demonstrated by multiple periodic measurements near 10 ppm NO_2. This finding suggests that the CS-0.7 sensor produces reliable, reproducible, reversible, and sequential outcomes for NO_2 detection. Furthermore, in comparison to metal oxide formaldehyde sensors, CdSe provides enhanced sensitivity, characterized by rapid response times, low operating temperatures, quick recovery times, and a reduced actual detection limit (refer to Table 2).

3.3. Mechanism analysis

The adsorption performance of NO_2 on CdSe surfaces containing Se vacancies were researched by first principles calculations based on density functional theory (DFT). As shown in Fig. S3, two adsorption sites (vacancy and Cd site next to vacancy) are considered. The adsorption energies of NO_2 at the vacancy and Cd sites are −0.31 eV and −0.61 eV, respectively, indicating stable adsorption of NO_2 at the Cd site. As shown in Fig. 5a, compared with the density of states of CdSe without vacancies, CdSe with vacancies exhibits significant defect states near the Fermi level. In addition, according to the changes in the DOS curve, it can be concluded that the introduction of vacancies affects the electronic environment of the surrounding atoms, leading to a wider charge redistribution. This charge redistribution and energy level reconstruction induced by vacancies effectively optimizes the electronic state of the material surface, reduces the energy barrier for NO_2 molecule adsorption, and greatly enhances gas sensing response. The Bader charge analysis results indicate that NO_2 acts as an electron acceptor to obtain 0.32 e from CdSe, which is consistent with the charge difference density calculation results in Fig. 5 (b, c).

CdSe is a typical n-type semiconductor, and its sensitivity mechanism is related to the charge transfer between the material and the target gas [60]. The sensing mechanism is primarily categorized into two stages (Fig. 5d). When CdSe is exposed to air, oxygen molecules will capture electrons from the conduction band of the material to form adsorbed oxygen ions, such as O_2^-, O^- and O^{2-} (eq.5-8) at varying temperatures [61], resulting in the formation of an electron depletion layer (EDL) on the surface. When the sensor is exposed to NO_2, there is a competitive relationship between NO_2 and O_2. The electron affinity of NO_2 is significantly higher than that of O_2 [62-64]. Based on the adsorption desorption equilibrium, NO_2 molecules preferentially adsorb on the surface of CdSe, resulting in an increase in resistance. In addition, NO_2 will react with adsorbed oxygen on the surface, leading to a further decrease in electron concentration within the CdSe material, expansion of the charge depletion layer [65], and an increase in resis-

Table 2. Comparison of NO_2 sensors performance.

Materials	Tem. (°C)	Con. (ppm)	Res.	T_{res}/T_{rec} (s)	Actual detection limit (ppm)	Refs.
WO_3	150	50	38%	82/325	1	[54]
CuO	100	5	67.1%		0.3	[55]
Cu-ZnO	200	100	326%	78/17	5	[56]
ZnO-CeO_2	120	1	20.74%	104/417.6	0.1	[57]
Pd-CuO	125	100	80%	72/98	5	[58]
NiO-WO_3	200	10	16.06	30/30	0.02	[59]
CS-0.7	120	10	9.03	5/10	0.1	This work

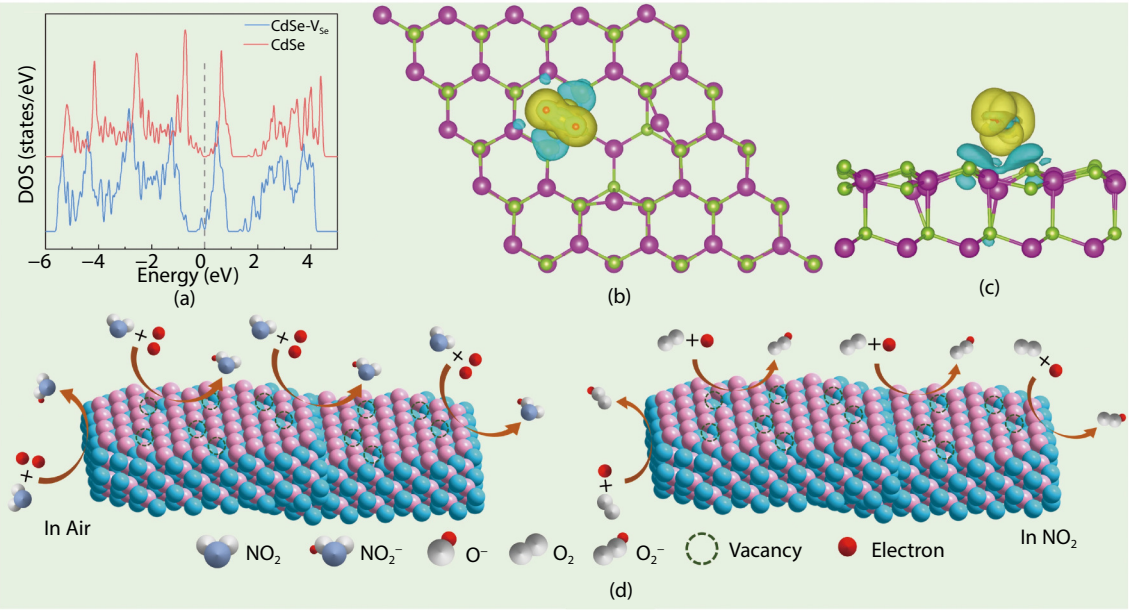

Fig. 5. (a) DOS curves before and after CdSe adsorption of NO_2, (b, c) charge differential density (The isosurface is set to 0.0004 e/Å^3.), (d) The sensing mechanism of CdSe sensors.

tance (eq.9-10).

$$O_{2(gas)} \rightarrow O_{2(ads)} \quad (5)$$

$$O_{2(ads)} + e^- \rightarrow O^-_{2(ads)} (T < 100^\circ C) \quad (6)$$

$$O^-_{2(gas)} + e^- \rightarrow 2O^-_{(ads)} (100^\circ C \leqslant T \leqslant 300^\circ C) \quad (7)$$

$$O^-_{(ads)} + e^- \rightarrow O^{2-}_{(ads)} (T > 300^\circ C) \quad (8)$$

$$NO_{2(ads)} + e^- \rightarrow NO^-_{2(ads)} \quad (9)$$

$$NO_2 + O^-_{(ads)} + 2e^- \rightarrow NO^-_{2(ads)} + O^{2-}_{(ads)} \quad (10)$$

Among the three CdSe gas sensors, the CS-0.7 sensor exhibits the best gas-sensing performance. The reason for the change of CdSe nanomaterials may be that adding an appropriate concentration of NaOH can reduce the grain size of CdSe, which is beneficial for gas-sensing response. As the grain size decreases, this increases the number of grains on the CdSe surface that are completely depleted in air, leading to an increase in surface defects and dangling bonds. These active sites can serve as catalytic centers for gas molecule adsorption and redox reactions [66]. The CS-0.7 sample has the highest lattice strain and dislocation density, as well as the smallest Nyquist curve radius (Fig. S4), which means it has the best charge mobility and more lattice defects. This can greatly improve gas sensing performance.

4. Conclusion

In summary, this work demonstrates that vacancy engineering is an effective strategy for constructing high-performance CdSe based NO_2 sensors. NaOH is included to manipulate the grain size and vacancy density in the CdSe samples, enhance interfacial charge transfer, and ensure uniform structural integrity. The alterations in grain size and vacancies of the CdSe were verified and tracked using XRD and EPR methods. The optimized CS-0.7 sensor attains a remarkable response (R_g/R_a = 9.04) for 10 ppm NO_2 at a temperature of 120°C with rapid kinetics (12/13 s for response/recovery), and it features an extensive dual-linear detection range of 0.1 to 30 ppm, outperforming many previously reported NO_2 sensors. Notably, the modifications in grain size and lattice strain improved the material's electronic mobility. The DFT calculation results show that the introduction of vacancies changes the electronic structure of CdSe, promotes surface electron redistribution, enhances the interaction between CdSe and NO_2, with an adsorption energy of −0.61 eV and an electron transfer of 0.32 e. These results position CdSe as a versatile model for developing high-accuracy gas sensors, with applications extending beyond NO_2 detection to innovative environmental sensing technologies.

Acknowledgements

This work was supported by the National Natural Science Foundation of China (62333008, 62273134), Program for Science & Technology Innovative Research Team in the University of Henan Province (25IRTSTHN005), Key R&D Special Project of Henan Province (241111322400), the Fundamental Research Funds for the Universities of Henan Province (NSFRF220101, NSFRF230432).

Conflict of interest

The authors declare no competing financial interest.

Electronic Supplementary Material (ESM)

The online version contains supplementary material available at https://doi.org/10.26599/ECS.2025.9600004.

References

[1] Tyagi, D.; Wang, H. D.; Huang, W. C.; Hu, L. P.; Tang, Y. F.; Guo, Z. N.; Ouyang, Z.; Zhang, H. Recent advances in two-dimensional-material-based sensing technology toward health and environmental monitoring applications. *Nanoscale*, 2020, 12: 3535–3559.

[2] Scheller, F. W., Zhang, X. R.; Yarman, A.; Wollenberger, U.; Gyurcsányi, R. E. Molecularly imprinted polymer-based electrochemical sensors for biopolymers. *Curr. Opin. Electrochem.*, 2019, 14: 53–59.

[3] Manzoor, S.; Talib, M.; Novikov, S. M., Arsenin, A. V., Volkov, V. S., Mishra, P. Physisorption-mediated charge transfer in TiS(2) nanodiscs: A room temperature sensor for highly sensitive and reversible carbon dioxide detection. *ACS Sens.*, 2023, 8: 3435–3447.

[4] Zeng, L. W.; Yang, J.; Guo, H.; Lyu, X. P. Impact of NO(x) reduction on long-term surface ozone pollution in roadside and suburban Hong Kong: Field measurements and model simulations. *Chemosphere*, 2022, 302: 134816.

[5] Ueda, T.; Boehme, I.; Hyodo, T.; Shimizu, Y.; Weimar, U.; Barsan, N. Effects of gas adsorption properties of an Au-loaded porous In_2O_3 sensor on NO_2-Sensing properties. *ACS Sens.*, 2021, 6: 4019–4028.

[6] Zhang, Z. Y.; Haq, M.; Wen, Z.; Ye, Z. Z.; Zhu, L. P. Ultrasensitive ppb-level NO_2 gas sensor based on WO_3 hollow nanosphers doped with Fe. *Appl. Surf. Sci.*, 2018, 434: 891–897.

[7] Liang, Z. P.; Zhang, X. Z.; Yang, J.; Cheng, Y.; Hou, H. G.; Hussain, S.; Liu, J. L.; Qiao, G. J.; Liu, G. W. Facile fabrication of nanoflower-like WO_3/WS_2 heterojunction for highly sensitive NO_2 detection at room temperature. *J. Hazard. Mater.*, 2023, 443: 130316.

[8] Wang, H. J.; Cui, Z.; Xiong, R.; Tang, L.; Ming, Y.; Wu, X.; Sa, B. S.; Song, W. L.; Zeng, D. W. Room temperature ultrasensitive NO_2 detection by activating VS2 basal planes in rare-earth Nd-doped VS2/carbon nanofibers. *ACS Materials Lett.*, 2024, 6: 2617–2625.

[9] Wang, T. T.; Wang, Y.; Fan, W. Q.; Wu, R. Z.; Liang, Q. H.; Hao, J. Y. Boosting room-temperature NO_2 detection *via in-situ* interfacial engineering on Ag_2S/SnS_2 heterostructures. *J. Hazard. Mater.*, 2022, 434: 128782.

[10] Qiu, H.; Liu, W. T.; Lin, S. Y.; Li, Z. Y.; He, Y. S.; Yim, S. H. L., Wong, E. L., Chuang, H. C.; Ho, K. F. Association of air pollution exposure with low arousal threshold obstructive sleep apnea: A cross-sectional study in Taipei, Taiwan. *Environ. Pollut.*, 2022, 306: 119393.

[11] Kushwaha, A.; Goel, N. Edge enriched MoS_2 micro flowered structure for high performance NO_2 sensor. *Sens. Actuat. B Chem.*, 2023, 393: 134190.

[12] Huang, X.; Li, Y. Z.; Liu, Y. H.; Peng, B.; Peng, J. Q.; Wang, G.; Mei, S.; Li, M. Y. Room temperature NO_2 sensor with rapid recovery based on ZnO/In_2O_3 heterojunction. *J. Mater. Sci. Mater. Electron.*, 2024, 35: 869.

[13] Bai, M. J.; Chen, M.; Li, X.; Wang, Q. J. One-step CVD growth of ZnO nanorod/SnO_2 film heterojunction for NO_2 gas sensor. *Sens. Actuat. B Chem.*, 2022, 373: 132738.

[14] Chang, J. N.; Qin, C.; Guo, W. J.; Zhu, L. H.; Zhang, Y.; Wang, Y.; Cao, J. L. Visible light enhanced NO_2 sensing performance of Au nanoparticles modified SnS_2 hierarchical structure at room temperature. *Sens. Actuat. B Chem.*, 2023, 385: 133633.

[15] Rao, C. N. R., Ramakrishna Matte, H. S. S., Maitra, U. Graphene analogues of inorganic layered materials. *Angew. Chem. Int. Ed.*, 2013, 52: 13162–13185.

[16] Neri, G. Thin 2D: The new dimensionality in gas sensing. *Chemosensors*, 2017, 5: 21.

[17] Cho, B.; Hahm, M. G., Choi, M.; Yoon, J.; Kim, A. R., Lee, Y. J.; Park, S. G.; Kwon, J. D.; Kim, C. S., Song, M. et al. Charge-transfer-based gas sensing using atomic-layer MoS_2. *Sci. Rep.*, 2015, 5: 8052.

[18] Liu, W.; Gu, D.; Li, X. G. Ultrasensitive NO_2 detection utilizing mesoporous ZnSe/ZnO heterojunction-based chemiresistive-type sensors. *ACS Appl. Mater. Interfaces*, 2019, 11: 29029–29040.

[19] Wu, H. Y.; Qi, L. X.; Song, B.; Tong, Y.; Li, L.; Ikram, M.; Shi, K. Y. $MoS_{2-x}Sex$ lamellae assembled with lotus-leaf-like structures for sensitive NO_2 gas sensors at room temperature. *Chem. Eng. J.*, 2024, 502: 157906.

[20] Yang, H. M.; Yang, Y. Z.; Ma, C. F.; Wu, Q. R.; Tang, J. H.; Zhu, C. Q.; Wang, X. X.; Zeng, D. W. Vacancy–assisted exposed Sn atoms enhancing NO_2 room temperature sensing of $SnSe_2$ nanoflowers. *Talanta*, 2024, 276: 126208.

[21] Liu, W. P.; Zhang, M.; Guo, L. A.; Peng, K. F.; Man, Z.; Xie, S. L.; Liu, P.; Xie, D.; Wang, S. S.; Cheng, F. L. Photoelectrochemical aptasensor based on nanocomposite of CdSe@SnS(2) for ultrasensitive and selective detection of sulfamethazine. *Mikrochim. Acta*, 2022, 189: 453.

[22] Li, C. Y.; Li, W. J.; Cheng, M. M.; Yang, W. Y.; Tan, Q. H.; Wang, Q. J.; Liu, Y. K. High sensitive and broadband photodetectors based on hybrid PbI_2 nanosheet/CdSe nanobelt. *Adv. Opt. Mater.*, 2021, 9: 2100927.

[23] Chen, X.; Li, J. Assembly and photocatalytic degradation activity of spherical ZnO/CdSe heterostructures on flexible carbon cloth substrates. *Nanomaterials*, 2022, 12: 1898.

[24] Fan, Z. B.; Liu, Y. F.; Guo, X.; Jin, Z. L. Construct organic/inorganic heterojunction photocatalyst of benzene-ring-grafted g-C_3N_4/CdSe for photocatalytic H_2 evolution. *Int. J. Hydrog. Energy*, 2023, 48: 19137–19152.

[25] Wu, Q.; Tian, L.; Shan, X. Y.; Li, H. L.; Yang, S. N.; Li, C.; Lu, J. An electrochemiluminescence sensor based on the CNTs and CdSe@ZnSe for determination of melamine in milk samples. *Food Chem.*, 2024, 430: 137028.

[26] Venci, X.; George, A.; Raj, A. D., Irudayaraj, A. A., Raj, D. M. A., Jayakumar, G.; Sundaram, S. J. Tuning the morphology and band gap of CdSe nanoparticles *via* solvothermal method. *Mater. Today Proc.*, 2021, 36: 459–463.

[27] Lv, R. G.; Ye, K.; Zhang, W. Y.; Chen, H. Y.; Zhao, R. F.; Wu, H. Y.; Chen, M. Homologous heterostructure CdSe/CdS nanoflowers to enhance photocatalytic hydrogen production. *Colloids Surf. A Physicochem. Eng. Aspects*, 2024, 684: 133143.

[28] Wang, W.; Zhang, Y. Y.; Zhang, J. N.; Li, G.; Leng, D. Y.; Gao, Y.; Gao, J. Z.; Lu, H. B.; Li, X. H. Metal–organic framework-derived Cu_2O–CuO octahedrons for sensitive and selective detection of ppb-level NO_2 at room temperature. *Sens. Actuat. B Chem.*, 2021, 328: 129045.

[29] Gao, W. J.; Wang, X.; He, Y.; Yu, H. H.; Zheng, Y.; Yin, R. C.; Jiang, X. Sub-ppm NO_2 gas sensing in CdTe quantum dots functionalized hollow-core anti-resonant fiber. *Sens. Actuat. B Chem.*, 2024, 405: 135350.

[30] Yan, R. T.; Zhao, W. J.; Duan, X. Y.; Yu, T. L.; Cui, W. P.; Quan, W. D.; Chen, Y. S.; Xu, D. The optimization of noble metal-modified $MoSe_2$ nanoflowers gas sensor for hazardous NO_2 detection. *Microchem. J.*, 2025, 209: 112892.

[31] Chen, G. X.; Xie, Z. M.; Qu, W. L.; Wang, D. D.; Zhang, Q.; Zhang, J. M. First-principles study of NO_2 adsorption on noble metals doped SnS_2/$SnSe_2$ heterostructure. *Comput. Theor. Chem.*, 2025, 1245: 115099.

[32] Liu, Y. M.; Zhang, Y.; Cao, J. L.; Qin, C.; Wang, Y. NiAl-LDHs-derived NiO/Al_2O_3 with high specific surface area for wide range hydrogen detection. *Int. J. Hydrog. Energy*, 2024, 85: 20–29.

[33] Rockland, L. B. Saturated salt solutions for static control of relative humidity between 5° and 40°C. *Anal. Chem.*, 1960, 32: 1375–1376.

[34] Wexler, A.; Hasegawa, S. Relative humidity-temperature relationships of some saturated salt solutions in the temperature range 0 degree to 50 degrees C. *J. Res. Natl. Bur. Stand.*, 1954, 53: 19.

[35] Hassan, M.; Liang, Z. P.; Liu, S. W.; Hussain, S.; Qiao, G. J.; Liu, G. W. Temperature-driven n- to p-type transition of a chemiresistive NiO/CdS-CdO NO_2 gas sensor. *Sens. Actuat. B Chem.*, 2024, 398: 134755.

[36] Nasiri, S.; Rabiei, M.; Palevicius, A.; Janusas, G.; Vilkauskas, A.; Nutalapati, V.; Monshi, A. Modified Scherrer equation to calculate crystal size by XRD with high accuracy, examples Fe_2O_3, TiO_2 and V_2O_5. *Nano Trends*, 2023, 3: 100015.

[37] Qin, C.; Wei, Z. X.; Wang, B.; Wang, Y. D. Sn and Mn co-doping synergistically promotes the sensing properties of Co_3O_4 sensor for high-sensitive CO detection. *Sens. Actuat. B Chem.*, 2023, 390: 133930.

[38] Dolabella, S.; Borzì, A.; Dommann, A.; Neels, A. Lattice strain and defects analysis in nanostructured semiconductor materials and devices by high-resolution X-ray diffraction: Theoretical and practical aspects. *Small Meth.*, 2022, 6: 2100932.

[39] Jiang, C. Y.; Zhang, L.; Gao, X. L.; Yu, W. Z.; Hu, C.; Tang, W. X.; Li, Z.; Cheng, L. L.; Wu, M. H. Se-vacancy porous ultrathin ZnSe nanosheet/carbon composite for sodium storage *via* electron beam irradiation strategy. *Chem. Eng. J.*, 2024, 497: 154936.

[40] Jiang, J. B.; Li, L.; Sun, R.; Wei, Y.; Xi, C.; Zhou, S. B.; Han, S.; Huang, X. Se vacancies and interface engineering modulated bifunctionality Prussian blue analogue derivatives for overall water splitting. *J. Colloid Interface Sci.*, 2025, 677: 904–921.

[41] Li, D. Y.; Hussain, S.; Wang, Y. J.; Huang, C.; Li, P.; Wang, M. Y.; He, T. ZnSe/CdSe Z-scheme composites with Se vacancy for efficient photocatalytic CO_2 reduction. *Appl. Catal. B Environ.*, 2021, 286: 119887.

[42] Huang, R. X.; Li, W. J.; Geng, L.; Dong, M.; Li, Y. J.; Fan, Y. Y.; Yang, L.; Liu, Y.; Han, H. L. Abundant active sites and excellent carrier separation synergistically enhanced hydrogen generation over NiS/CdSe Schottky heterojunction photocatalysts. *Int. J. Hydrog. Energy*, 2024, 89: 898–906.

[43] Sing, K. S. W. Reporting physisorption data for gas/solid systems with special reference to the determination of surface area and porosity (Recommendations 1984). *Pure Appl. Chem.*, 1985, 57: 603–619.

[44] Chang, J. N.; Qin, C.; Zhang, Y.; Zhu, L. H.; Zhang, Y.; Wang, Y.; Cao, J. L. Abundant active sites triggered by Co-doped SnS_2 for ppb-level NO_2 detection. *Sens. Actuat. B Chem.*, 2023, 395: 134511.

[45] Liang, J. X.; Zou, Z. S.; Zhao, Z. H.; Hui, B.; Tian, W. L.; Zhang, K. W. Intelligent gas detection: G-C_3N_4/polypyrrole decorated alginate paper as smart selective NH_3/NO_2 sensors at room temperature. *Inorg. Chem.*, 2024, 63: 12516–12524.

[46] Zhang, Z. Q.; Liang, J. X.; Liu, K.; Tian, W. L.; Liang, X.; Zhao, K.; Zhang, K. W. Defect-engineered WO(3-x) architectures coupled with random forest algorithm enables real-time seafood quality assessment. *ACS Sens.*, 2024, 9: 4196–4206.

[47] Liu, K.; Xu, Y. F.; Tian, X. Z.; Liang, J. X.; Zhao, Z. H.; Wang, J.; Zhang, Z. Q.; Zhang, K. W.; Yang, S. Stacking growth of ionically conductive MOF on biofabrics enables reliable NH_3 sensor for hepatic encephalopathy diagnosis. *npj Flex. Electron.*, 2025, 9: 67.

[48] Liu, J. Q.; Lv, J. R.; Xiong, H. M.; Wang, Y. J.; Jin, G. H.; Zhai, Z. X.; Fu,

C.; Zhang, Q. R. Size effect and comprehensive mathematical model for gas-sensing mechanism of SnO_2 thin film gas sensors. *J. Alloys Compd.*, 2022, 898: 162875.

[49] Li, Y. W.; Luo, N.; Sun, G.; Zhang, B.; Jin, H. H.; Lin, L.; Bala, H.; Cao, J. L.; Zhang, Z. Y.; Wang, Y. Synthesis of porous nanosheets-assembled ZnO/$ZnCo_2O_4$ hierarchical structure for TEA detection. *Sens. Actuat. B Chem.*, 2019, 287: 199–208.

[50] Yu, C. Y.; Liu, J. H.; Zhao, H. C.; Wang, M. Q.; Li, J.; She, X. P.; Chen, Y.; Wang, Y. J.; Liu, B. C.; Zou, C. et al. Sensitive breath acetone detection based on α-Fe_2O_3 nanoparticles modified WO_3 nanoplate heterojunctions. *IEEE Trans. Instrum. Meas.*, 2024, 73: 9513908.

[51] Sun, M. J.; Ding, K.; Lu, Y. J.; She, X. P.; Chen, Y.; Wang, M. Q.; Zou, C.; Liu, X. Y.; Zhou, Y. Two-dimensional p-n heterojunctions of black phosphorus nanosheet-sensitized α-MoO_3 nanoflake for low-temperature chemiresistive NH_3 recognition. *Microchem. J.*, 2024, 207: 111911.

[52] Cai, Y. H.; Ma, S. Y.; Wei, J. S. Highly sensitive triethylamine sensor with ppb level detection limit based on SnSe nanofibers. *Ceram. Int.*, 2023, 49: 15333–15340.

[53] Tan, X. Y.; Wang, L.; Chen, X.; Zhang, H. L.; Chen, S.; Qian, L. B.; Chen, Z. Y.; He, C. Q. A heterojunction composite of Bi_2Se_3 nanosheets and MoO_3 nanobelts for a high-performance triethylamine sensor. *J. Mater. Chem. C*, 2023, 11: 16356–16367.

[54] Rani, S.; Dahiya, R.; Kumar, V.; Berwal, P.; Sihag, S. Hydrothermally engineered WO_3 nanosheets as potential NO_2 gas sensor. *Ionics*, 2025, 31: 993–1002.

[55] Sihag, S.; Dahiya, R.; Rani, S.; Berwal, P.; Jatrana, A.; Sisodiya, A. K., Sharma, A.; Kumar, V. Low ppm NO_2 detection through advanced ultrasensitive copper oxide gas sensor. *Discov. Nano*, 2024, 19: 107.

[56] Kamble, V. S.; Zemase, R. K.; Gupta, R. H.; Aghav, B. D.; Shaikh, S. A.; Pawara, J. M.; Patil, S. K.; Salunkhe, S. T. Improved toxic NO_2 gas sensing response of Cu-doped ZnO thin-film sensors derived by simple co-precipitation route. *Opt. Mater.*, 2022, 131: 112706.

[57] Sun, K.; Zhan, G. H.; Chen, H. D.; Lin, S. W. Low-operating-temperature NO_2 sensor based on a CeO(2)/ZnO heterojunction. *Sensors*, 2021, 21: 8269.

[58] Ambedkar, A. K., Gautam, D.; Vikal, S.; Singh, M.; Kumar, A.; Sanger, A.; Sharma, K.; Singh, B. P., Gautam, Y. K. Ocimum sanctum leaf extract-assisted green synthesis of Pd-doped CuO nanoparticles for highly sensitive and selective NO_2 gas sensors. *ACS Omega*, 2023, 8: 29663–29673.

[59] Li, Q. Y.; Zhang, P.; Ning, T. G.; Sun, Y. S.; Ren, Q. Q.; Xu, M. Z.; Zhao, X. Y.; Luo, X. L.; Zhai, C. X.; Yan, J. F. et al. Gas sensor based on flower-like NiO modified with WO_3 nanoparticles for NO_2 detection. *ACS Appl. Nano Mater.*, 2024, 7: 7856–7864.

[60] Li, Y.; Wei, X. Y.; Liu, Q. Y.; Zang, D. M.; You, R. Visible light-activated room temperature NO_2 gas sensing based on the In_2O_3@ZnO heterostructure with a hollow microtube structure. *ACS Sens.*, 2024, 9: 3741–3753.

[61] Nguyen, T. K.; Jeong, S.; Youn, J. S.; Ahn, S.; Nam, K. H.; Park, C. M.; Jeon, K. J. Insight into mechanism of temperature-dependent limit of NO_2 detection using monolayer MoS_2. *Sens. Actuat. B Chem.*, 2021, 329: 129138.

[62] Yang, W. L.; Zhao, C. J.; Du, B. S.; Wu, R.; Lai, X. F.; He, Y.; Jian, J. K. SnSe nanosheet arrays film for trace NO_2 detection at room temperature. *Sens. Actuat. B Chem.*, 2022, 370: 132407.

[63] Li, J.; Yang, M.; Li, Y. Y.; Cheng, X. L.; Zhang, X. F.; Xu, Y. M.; Gao, S.; Zhao, H.; Huo, L. H. Construction of SnO_2 nanoneural network by ultrasmall particles for highly selective NO_2 detection at low temperature. *Sens. Actuat. B Chem.*, 2022, 361: 131703.

[64] Wu, M. J.; Wu, Y. Z.; Tung, Y. F.; Chang, T. C.; Lee, C. T.; Lee, H. Y. Surface modification and decoration of nano-honeycombed ZnO structure with gold-black nanoparticles for high responsivity detection of NO_2 gas sensors. *IEEE Sens. J.*, 2024, 24: 38699–38707.

[65] Li, R. X.; Wang, Q.; Wang, Y. R.; An, B. X.; Yang, Y. F.; Wu, Z. K.; Wang, P. Z.; Zhang, T. Y.; Han, R. Q.; Xie, E. Q. Unraveling the effect of oxygen vacancy on WO_3 surface for efficient NO_2 detection at low temperature. *ACS Appl. Mater. Interfaces*, 2024, 16: 51738–51747.

[66] Kim, S.; Carpenter, P. D., Jean, R. K., Chen, H. T.; Zhou, C. W.; Ju, S.; Janes, D. B. Role of self-assembled monolayer passivation in electrical transport properties and flicker noise of nanowire transistors. *ACS Nano*, 2012, 6: 7352–7361.